



Role of defect relaxation for trap-assisted tunneling in high- κ thin films: A first-principles kinetic Monte Carlo study

Gunther Jegert,^{*} Dan Popescu, and Paolo Lugli

Institute for Nanoelectronics, TU Munich, D-80333 Munich, Germany

Martin Johannes Häufel[†]

Institute of Physical Chemistry, University of Zurich, CH-8057 Zurich, Switzerland

Wenke Weinreich

Fraunhofer Center Nanoelectronic Technology, D-01099 Dresden, Germany

Alfred Kersch

University of Applied Sciences Munich, D-80335 Munich, Germany

(Received 2 August 2011; published 5 January 2012)

We assess the impact of structural relaxation of defects upon charging on trap-assisted tunneling in high- κ dielectric materials. $\text{ZrO}_2/\text{Al}_2\text{O}_3/\text{ZrO}_2$ thin films are taken as an exemplary system. In our completely different approach, a first-principles defect model is derived from Hedins GW approximation calculations, which is then coupled to kinetic Monte Carlo charge transport simulations. Comparison between simulation and experiment demonstrates that it is often imperative to take structural relaxation processes into account when modeling nanoscale transport across defect states.

DOI: [10.1103/PhysRevB.85.045303](https://doi.org/10.1103/PhysRevB.85.045303)

PACS number(s): 73.50.-h, 73.61.-r, 05.10.Ln, 84.32.Tt

I. INTRODUCTION

For decades, semiconductor bulk defects have been the subject of intensive studies,¹ and it is common knowledge that the energy of defect levels depends on the defect charge state.² Electrostatic interactions between charges localized at defect sites and the surrounding lattice atoms lead to structural relaxation. The atoms in the vicinity of the defect undergo a rearrangement in order to minimize the total energy of the system. Remarkable shifts of atoms, and thus, defect levels, can be observed; a prominent example being the bistability of the oxygen vacancy in SiO_2 (E' center) (Ref. 3).

While known for a long time, the influence of the structural relaxation of defects, caused by a change in their charge states, on charge transport across defect states, scarcely has been addressed.⁴ Especially, in modern nanoscale devices, featuring film thicknesses below 10 nm, unanticipated effects may arise. This is to be expected for high- κ oxides, a different class of materials that, in past years, has attracted a lot of interest in the research community. Used as dielectrics in the state-of-the-art transistor gate stack,⁵ in future carbon-nanotube transistors,⁶ and in the storage capacitor of dynamic random access memories (DRAMs),⁷ high- κ materials are of utmost importance for the semiconductor industry. Stringent requirements on their insulating properties are set in order to ensure a satisfactory device performance. Especially, for the DRAM capacitor, leakage currents as low as 10^{-7} A/cm² at operating conditions (1 V, 125 °C) are needed. However, it is well known that the high- κ oxides, due to their large coordination, suffer from high-defect densities.⁸ This has triggered numerous studies of defect levels in materials, such as HfO_2 , ZrO_2 , TiO_2 , and SrTiO_3 ,^{9–12} which incidentally has demonstrated that structural relaxation has a strong effect on the energy of defect levels in high- κ oxides.

Currently employed high- κ layers are still too thick to observe direct quantum-mechanical tunneling through the dielectrics. Nonetheless, a noteworthy current flow across these films is observed. In view of the high-defect densities, trap-assisted tunneling (TAT), i.e., transport across defect states in the oxide band gap, has been demonstrated.¹³ Obviously, as soon as charges flow across defects, causing frequent changes in the defect charge states, defect relaxation will strongly influence the electronic transport. Surprisingly, however, the impact of defect relaxation on TAT has been neglected in transport models set up so far (e.g., Refs. 14 and 15).

Considering the current stand of the semiconductor industry, which, only a few years after successful integration of high- κ dielectrics, is pushing these materials to their scaling limits,¹⁶ a better understanding of the charge transport is crucial. In fact, further scaling of integrated circuits, i.e., usage of thinner high- κ films, requires full control and optimization of their insulating properties. Envisaging the current downscaling speed, a value of 0.4 nm for the equivalent oxide thicknesses (EOTs) will be required within the next 2 yr (according to the *International Technology Roadmap for Semiconductors*¹⁷). Yet no feasible concept is known that fulfills the strict leakage current criteria for the DRAM storage capacitor and, at the same time, enables such low EOTs. A huge effort is undertaken to develop manufacturable solutions providing ultralow EOTs, whereas the focus is laid on SrTiO_3 (Refs. 18–20) and rutile TiO_2 (Ref. 21) in combination with Ru-based electrodes since these materials provide permittivities of more than 100.

Other classes of materials have been suggested, as, for instance, trilaminate $\text{ZrO}_2/\text{Al}_2\text{O}_3/\text{ZrO}_2$ (ZAZ) dielectrics,^{22–24} used in the latest chip generations. Here, two polycrystalline layers of tetragonal ZrO_2 ($t\text{-ZrO}_2$), featuring a permittivity close to 40, surround a thin (~ 0.5 -nm) amorphous Al_2O_3

interlayer, which improves the insulating properties compared to pure ZrO_2 films.²² The actual reason for this improvement is still a subject of discussion. It was suggested that the interlayer prevents ZrO_2 grains from extending over the whole dielectric and causing excessive surface roughness,²⁵ which is known to have a detrimental effect on the capacitor performance.²⁶ It also was argued qualitatively that the large band gap of Al_2O_3 sets up a barrier for charge flow.²³ However, a quantitatively predictive model for the leakage currents in $\text{TiN}/\text{ZrO}_2/\text{Al}_2\text{O}_3/\text{ZrO}_2/\text{TiN}$ (TZAZT) capacitors is still missing. The fact that structural relaxation of defects easily causes energetic shifts in the defect levels larger than 1 eV (Ref. 27) strongly suggests that relaxation processes have to be accounted for in this context.

In the past, we have established a framework for transport simulations based on kinetic Monte Carlo (kMC). kMC has been used to model leakage currents in high- κ thin-film capacitors,^{13,28} a system where a large diversity of mutually interdependent transport mechanisms has to be taken into account. Here, we study electronic transport in TZAZT capacitors by coupling our kMC algorithm to a defect model derived from first-principles Hedins GW approximation (GW) calculations. The impact of structural relaxation of defects and the accompanying change of the defect-energy levels on charge-carrier transport is investigated, and a complete transport model for these devices is developed, intended to support the experimental efforts toward optimization of these devices.

II. DEFECT MODEL

As said, many elaborate studies of defect levels in the high- κ materials are available. To save computation time, usually defect levels are calculated in the local-density approximation (LDA), i.e., the results suffer from the systematically underestimated band gap. While precise rules for rescaling the band gap are known, due to the rescaling process, the energy of the defect levels within the band gap is afflicted with some uncertainty. For an unambiguous identification of structural defects, which might constitute the dominant leakage current channels, a more accurate analysis is needed. Alternative calculation schemes exist, which are, on one hand, much more costly but on the other hand, deliver very precise results for defect-level energies. One of these methods is the GW approximation^{29,30} in which dynamical screening effects are taken into account, leading to better results for the band

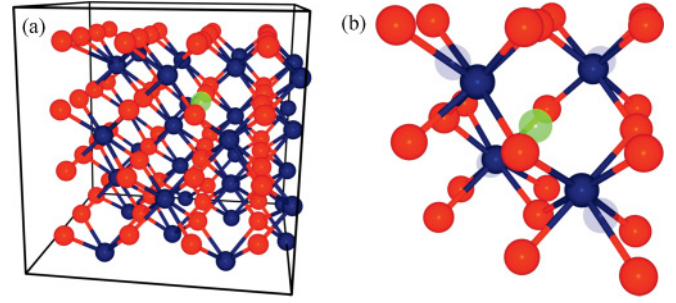


FIG. 1. (Color online) (a) A 95-atom supercell of $t\text{-ZrO}_2$ used to perform the GW calculations. O atoms are shown in light red, Zr atoms are shown in dark blue. An oxygen vacancy was formed by removing one oxygen atom (green). Subsequently, the atomic structure was relaxed. (b) Zoom on the direct vicinity of the oxygen vacancy (missing O atom is colored green). The relaxed structure for the neutral vacancy V_O^0 is pictured. Semitransparent dark blue balls show the positions of the nearest-neighbor Zr atoms for the positively charged vacancy. Upon removal of an electron, the Zr atoms are pushed away from the vacancy by the localized positive charge. For better visibility, the displacement is upscaled by a factor of 5.

gap and excited states of many semiconducting and insulating materials.^{30,31}

By means of GW calculations, we study oxygen vacancies in $t\text{-ZrO}_2$, a common defect in this material³² and the most probable candidate for causing the leakage currents in this dielectric. Calculations are carried out using a $2 \times 2 \times 2$ supercell consisting of 95 atoms as shown in Fig. 1(a). In Table I, the results of the defect-level calculations are presented along with published theoretical values. These defect levels, i.e., the Kohn-Sham orbitals within the band gap, can be interpreted as a close approximation of experimentally observable ionization potentials and electron affinities.³³

Defect formation enthalpies were calculated for the LDA and the GW approximation, as described in Ref. 34. As Fig. 2 shows, for relevant Fermi energies, determined by the TiN electrode Fermi level, the prevailing charge states for oxygen vacancies (V_O) are neutral (V_O^0), positive (V_O^+), and twofold positive (V_O^{++}). Electrical neutrality of the dielectric is ensured either by negatively charged defects within the dielectric or by delocalized electrons. In the latter case, where the oxygen vacancies act as donors, an electron density of 10^{20} cm^{-3} would lead to a band bending of approximately 0.1 eV. Such compensation effects were neglected in the course of our studies.

TABLE I. Defect-energy levels of the neutral and of charged oxygen vacancies in $t\text{-ZrO}_2$ (in eV) in comparison to published theoretical results. We give the energy difference for the conduction-band (CB) minimum in parentheses.

Charge state	This paper		Theoretical		
	LDA	GW	$t\text{-ZrO}_2$ from Ref. 35	$m\text{-ZrO}_2$ from Ref. 36	$c\text{-ZrO}_2$ from Ref. 37
-1	2.58 (0.94)	2.59 (2.94)	2.40 (4.20)		
-1	3.49 (0.03)	5.00 (0.53)	4.40 (2.20)		
Neutral	0.96 (2.56)	3.06 (2.44)	3.35 (3.55)	2.20	3.45 (2.1)
+1 (spin up, occupied)	0.68 (2.84)	3.08 (2.43)	4.20 (2.70)		
+1 (spin down, unoccupied)	3.41 (0.11)	4.41 (1.09)	6.10 (0.80)		
+2	3.48 (0.04)	5.25 (0.27)	7.00 (-0.10)		

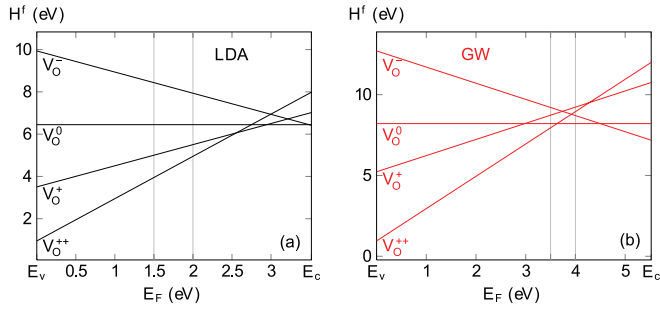


FIG. 2. (Color online) Formation enthalpies H^f of neutral and charged oxygen vacancies in t - ZrO_2 as a function of the Fermi energy E_F , calculated (a) using LDA total energies and (b) using an approach that includes GW electron affinities.³⁴ The Fermi energy of the TZAZT system is pinned by the TiN electrodes to 1.5–2 eV below the CB minimum (ranges marked by vertical lines).

The position of the corresponding defect-energy levels of the relaxed oxygen vacancy within the band gap of t - ZrO_2 is shown in Fig. 3.

For V_O^0 , two degenerate filled defect levels are found 2.44 eV below the ZrO_2 CB, corresponding to two electrons that are localized strongly at the vacancy site. Upon removal of an electron (V_O^+), the now unoccupied spin-down state (β) moves up to 1.09 eV, while the occupied spin-up state (α) remains energetically unaffected. For the neutral oxygen vacancy, screened Coulomb repulsion between the two localized electrons, as described by Eq. (1) below, leads to a potential-energy contribution on the order of 0.3–0.5 eV. Thus, upon removal of one electron, one would expect the defect-energy level to shift downward by this amount. However, upon positive charging of the defect, a large structural relaxation takes place. Figure 1(b) shows a closeup view of the relaxed atomic structure in the vicinity of a neutral oxygen vacancy V_O^0 . If one electron is removed, the remaining positive charge localized at the vacancy site forces the positive Zr ions to relax 0.11 Å away from the vacancy. (The resulting Zr positions are shown as semitransparent blue balls.) Thus, the attractive potential energy between the remaining electron and the Zr

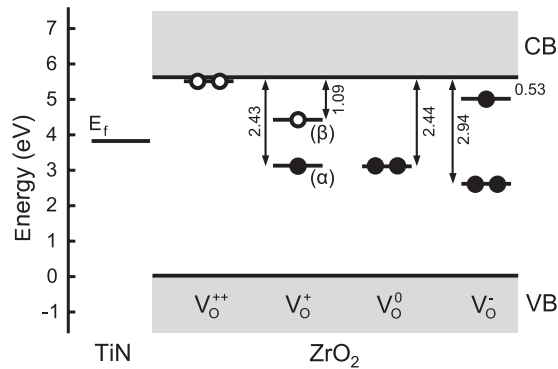


FIG. 3. Energy-level diagram showing the positions of the oxygen vacancy states within the t - ZrO_2 band gap. All defect-energy levels were obtained using the GW approximation; all values are given in electron volts (eV). For V_O^+ , the nondegenerate spin-up and spin-down states are denoted (α) and (β), respectively. Open (closed) circles denote unoccupied (occupied) states.

ions decreases, causing the (α) state to more or less remain energetically unchanged and the unoccupied (β) state to shift 1.35 eV upward. A similar value of 0.10 Å for the relaxation distance was found in Refs. 10 and 35. However, in Ref. 10, the exchange correlation was described by the generalized gradient approximation leading to a defect-level shift of only 0.6 eV, while embedded cluster calculations in Ref. 35, overestimating the ZrO_2 band gap, found a shift of 2.75 eV. By removing another electron (V_O^{++}), the two unoccupied states move up close to the CB.

III. KMC FRAMEWORK

The defect model (Fig. 3), derived from the GW calculations, was subsequently incorporated into a kMC algorithm to study the effect of the structural relaxation on the electronic transport.

To get a correct picture of the electron transport and, especially, the statistical interplay of different transport mechanisms, all relevant electron transitions—hole transport is negligible in the TiN/ ZrO_2 system¹³—have to be taken into account concurrently. The set of transport mechanisms included in the kMC simulations is sketched in Fig. 4. These encompass both electrode-limited mechanisms, such as (i) direct tunneling and (ii) Schottky emission as well as bulk-limited mechanisms, such as (iii) elastic or inelastic tunneling of electrons into and (iv) out of defects, (v) Poole-Frenkel emission, i.e., thermal emission of electrons from defects over a barrier reduced by the present electrical field into the CB, and (vi) tunneling between defects. In addition, we self-consistently integrate (vii) structural relaxation of defects upon a change in their charge state, causing a shift in the defect-energy level. In general, we assume that transitions of types (iii)–(vii) exist for every single defect and, thus,

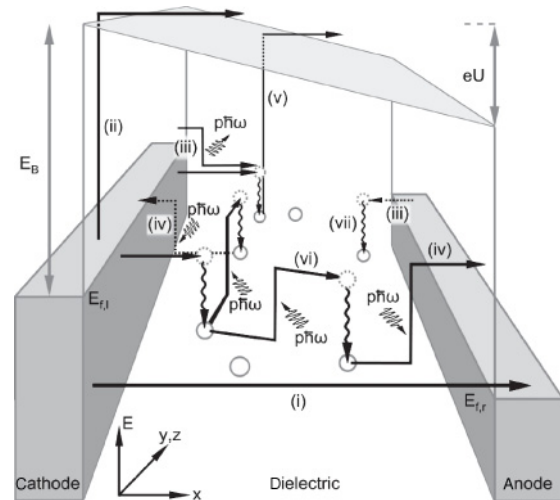


FIG. 4. Schematic band diagram of a metal-insulator-metal structure with applied voltage U . Transport mechanisms, implemented in the kMC simulator: (i) direct or Fowler-Nordheim tunneling, (ii) Schottky emission, (iii) elastic and inelastic tunnelings (p = number of phonons with energy $\hbar\omega$) into and (iv) out of defects, (v) Poole-Frenkel emission, (vi) defect-defect tunneling, and (vii) structural relaxation of a defect upon a change in its charge state (waved arrows).

TABLE II. Model parameters for the individual layers of the ZAZ dielectric used in the kMC simulations. For comparison, measured values, only available for the whole dielectric stack, are given in parentheses.

Samples	Layer thicknesses (nm)				Layer permittivities			
	Bottom ZrO ₂	Al ₂ O ₃	Top ZrO ₂	ZAZ Stack	Bottom ZrO ₂	Al ₂ O ₃	Top ZrO ₂	ZAZ Stack
T7ZAZT	3.4	0.5	3.4	7.3 (7.3)	38	9	38	31.1(31.4)
T9ZAZT	4.5	0.4	4.5	9.4 (9.4)	38	9	38	33.4(35.2)

constitute parallel electron-transport channels that influence each other.

The physical models for the different transport mechanisms are an essential input of our kMC simulations. They are taken from Ref. 13 for transitions (i)–(vi).

In order to account for the structural relaxation of the defects due to a change in their charge state, the defect model is coupled to the kMC simulations by setting the defect energies for different charge states to the GW values. It turns out that the residence time of electrons in the defects is orders of magnitude larger than the time needed for structural relaxation (in the picosecond regime³⁸) around the defect after a change in the charge state. Thus, we neglected relaxation time in our simulations, i.e., for transitions of type (vii), we assumed a rate $R_{\text{relax}} \rightarrow \infty$.

The electrostatic potential in the vicinity of charged defects was modeled as a screened Coulomb potential. For defect i with electrical charge Ze , located at position \vec{r}_i , it can be written as

$$V(\vec{r}) = \frac{Ze}{4\pi\epsilon_{\text{opt}}\epsilon_0|\vec{r} - \vec{r}_i|}. \quad (1)$$

Here, Z is an integer number, giving the charge state of the defect, and ϵ_{opt} is the optical permittivity of the surrounding dielectric material, taken as 5.6 in ZrO₂ (Ref. 39).

IV. SAMPLE PREPARATION

The above-described first-principles kMC simulator was used to simulate charge transport in planar TZAZT capacitors, which were fabricated as follows. First, silicon wafers were coated with chemical vapor-deposited (CVD)

TiN (TiCl₄, NH₃) at 550 °C. Then, ZrO₂ and Al₂O₃ layers were formed by atomic layer deposition from (TEMAZ, O₃) and [Al(CH₃)₃, O₃], respectively, at 275 °C. A postdeposition anneal at 650 °C in N₂ was carried out prior to TiN top electrode deposition at 450 °C by CVD. Current measurements were carried out with a Keithley 4200 parameter analyzer.⁴⁰ Total film thicknesses were determined via spectroscopic ellipsometry, and the effective permittivities of the ZAZ stacks were extracted from capacitance measurements. The experimental values are given in Table II and are in excellent agreement with our model.

V. LEAKAGE CURRENT SIMULATIONS

Figure 5 shows the leakage current data of the two capacitor structures for temperatures between 25 °C and 150 °C as a function of the mean-electric field $\langle F \rangle = U/d$ with the applied bias U and the total dielectric stack thickness d . In order to study the effect of structural relaxation on electron transport in these thin-film capacitors by means of kMC, some assumptions had to be made, whose justification will be commented on later. For the sake of simplicity, it was assumed that one single type of defect, homogeneously distributed within the dielectric, causes the dominant leakage current contributions.

Best-estimate physical parameters, entering the kMC transition rates, were taken to characterize the dielectric stack and were kept fixed during the simulations. They are listed in Ref. 13. Assumed thicknesses and permittivities of the individual ZrO₂ and Al₂O₃ layers, given in Table II, were chosen so as to reproduce the measured total film thicknesses and permittivities of the ZAZ laminates. The only fitting

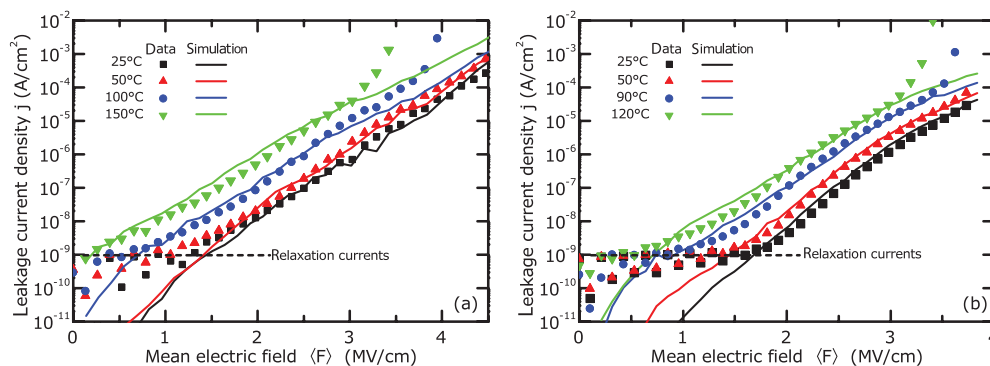


FIG. 5. (Color online) Leakage current data (symbols) of TZAZT capacitors with dielectrics of (a) 7-nm and (b) 9-nm thicknesses compared to kMC simulation results (lines). In the low-field region, the measured current is dominated by transient relaxation currents, while the kMC results describe the steady state, thus, no comparison is possible.²⁸ Dielectric breakdown was observed for high fields.

parameters are the CB offset E_B at the TiN/ZrO₂ interface and the defect density.

In this model framework, we found a single set of parameters that accurately reproduces both the temperature and the thickness scaling of the leakage current as can be seen in Figs. 5(a) and 5(b). The closest fit to the experimental data was achieved for a barrier height of 1.9 eV, a value that compares well to an earlier result of 1.74 eV (Ref. 13) and theoretical estimates. Assuming a work function of 4.7 eV for TiN (Ref. 41) and for ZrO₂, an electron affinity of 2.5 eV, and a charge-neutrality level⁴² of 3.6 eV, the estimates lie between 1.45 eV according to the metal-induced gap-states model⁴² and 2.2 eV in the Schottky limit.

For the best possible fit of the kMC simulations to the experimental data, the defect-level energies for the different charge states were changed slightly with respect to the GW values (given in parentheses) to $E_{d,(\beta)}^+ = 1.1$ eV (1.09 eV) for the unoccupied (β) state of the positively charged vacancy and $E_d^0 = 2.3$ eV (2.44 eV) for the degenerate states of the neutral defect with respect to the CB. The energies of the unoccupied states of the twofold positively charged defect and the occupied (α) state of the positively charged defect were left unchanged. These minor changes lie well within the error margin of the GW results.

In the course of our studies, we systematically varied the energy of the defect state and its relaxation energy, however, without achieving a good fit of the experimental data. Also, the assumption of several types of defects being present at the same time did not allow reproducing the experimental data. From all this, we draw the conclusion that, indeed, structural

relaxation is essential to explain the electron transport in TZAZT capacitors and that oxygen vacancies are responsible for the dominant leakage current contribution.

VI. TRAP-ASSISTED TUNNELING ACROSS OXYGEN VACANCIES

From the kMC simulations, the following picture of electron transport across the dielectric, as shown in Fig. 6, emerges. An electron is injected from the TiN electrode into the unoccupied electron state of a positive vacancy 1.1 eV below the ZrO₂ CB [Fig. 6(a)], which subsequently relaxes by $E_{\text{relax}} = E_d^0 - E_{d,(\beta)}^+ = 1.2$ eV [Fig. 6(b)]. The trapped electron then moves by phonon-assisted tunneling into a neighboring positively charged vacancy [Fig. 6(c)], which again relaxes. In this way, percolating along a chain of oxygen vacancies, the electron crosses the dielectric [Fig. 6(d)]. The number of percolation sites varies between 1 and 3, depending on film thickness and applied bias. (The thinner the dielectric and the higher the applied bias, the fewer the sites needed.)

Earlier models that neglected structural relaxation effects came to the conclusion that transport, while being dominated by TAT at lower voltages, could be explained by Poole-Frenkel conduction at higher voltages^{14,15,28} via a defect level located, e.g., 1.15 eV (Ref. 28) below the CB. Our *ab initio* analysis shows that this corresponds almost exactly to the relaxation energy E_{relax} of the oxygen vacancy. Such a coincidence explains why, in both models, a similar temperature scaling of the leakage current is obtained. Clearly, only the model including structural relaxation effects is consistent with first-principles

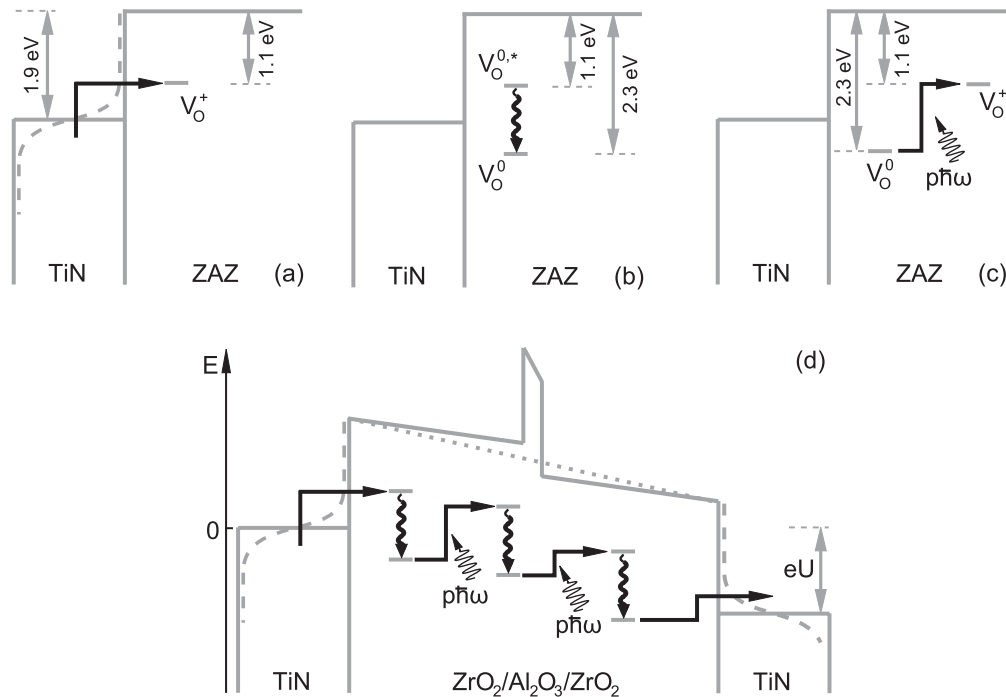


FIG. 6. The different steps of an electron crossing the dielectric film are sketched. (a) First, the electron is injected into a positive oxygen vacancy that (b) subsequently undergoes structural relaxation causing the defect-energy level to shift downward. (c) In the next step, the electron moves via an inelastic multi-phonon-assisted transition to a neighboring positively charged oxygen vacancy. (d) By repeating the last two steps, the electron can percolate along a chain of defect states until finally, it is emitted to the counterelectrode. Here, p is the number of phonons with energy $\hbar\omega$.

defect-level calculations as shown here and in Refs. 10 and 35. Based on the calculated defect levels of the oxygen vacancy, which, for the relevant charge states, lie much deeper in the band gap (≈ 2.4 eV), Poole-Frenkel conduction is ruled out as a dominant transport mechanism since the rate for Poole-Frenkel emission of an electron from a defect state [Eq. (10) in Ref. 13] is reduced by 1 order of magnitude every 0.1 eV of defect depth.

Best quantitative matching of the simulations with the experimental data was achieved for a defect concentration of $1 \times 10^{20} \text{ cm}^{-3}$. Such a high concentration might be due to the presence of the high work-function TiN electrodes, which are known to increase the concentration of oxygen vacancies in such high- κ thin films.⁴³ Via soft x-ray photoelectron spectroscopy, defect densities in the range of 2×10^{19} to $1 \times 10^{20} \text{ cm}^{-3}$ were estimated.⁴⁴ The investigation of $(\text{ZrO}_2)_{0.8}(\text{Al}_2\text{O}_3)_{0.2}$ films via conductive atomic force microscopy⁴⁵ suggests that transport predominantly occurs along grain boundaries in the polycrystalline ZrO_2 . Since oxygen vacancies are known to cluster at grain boundaries,^{44,46} such experimental evidence strongly suggests that they are responsible for opening the loss paths.

VII. CONCLUSIONS

To summarize, multistep inelastic phonon-assisted tunneling across oxygen vacancies has been identified as the dominant conduction mechanism in TZAZT capacitors. A closed model, taking structural relaxation of the involved defects upon a change in their charge states into account, was presented. Consideration of defect relaxation leads to a qualitative modification of our picture of electron transport. Instead of Poole-Frenkel conduction, trap-assisted tunneling across oxygen vacancies is identified as the dominant transport mechanism.

ACKNOWLEDGMENTS

We would like to acknowledge the financial support of the German Excellence Initiative via the Nanosystems Initiative Munich (NIM) and the Deutsche Forschungsgemeinschaft.

APPENDIX

1. GW calculations

In the GW approach, crystal electrons are viewed to be surrounded by a polarization cloud. Thus, a screened interaction with the other electrons takes the place of bare Coulomb interaction. Therefore, the excitations of the many-particle system can be described as those of weakly interacting quasiparticles.

The GW approximation can be written formally as an expansion of the self-energy Σ , defined as the energy difference between the quasiparticle and the bare electron, in terms of the screened interaction W ,

$$\Sigma \approx GW, \quad (\text{A1})$$

where G denotes the single-particle Green's function. In Feynman diagram representation, this reads

(A2)

The equation of motion is given by the quasiparticle equation,

$$h\Psi_i(\mathbf{r}) + \int d^3r' \Sigma(\mathbf{r}, \mathbf{r}'; E_i)\Psi_i(\mathbf{r}') = E_i\Psi_i(\mathbf{r}), \quad (\text{A3})$$

where h is the one-particle Hamiltonian in the Hartree approximation and Ψ_i and E_i are the quasiparticle wave function and energy, respectively. In this definition, the self-energy contains all the exchange and correlation contributions beyond the Hartree approximation. Note that, for simplicity, spin degrees of freedom are neglected in this presentation, whereas the actual calculations are carried out in a spin-polarized way. Comparing the quasiparticle equation to the Kohn-Sham equations,

$$[h + v_{xc}(\mathbf{r})]\varphi_i(\mathbf{r}) = \varepsilon_i\varphi_i(\mathbf{r}), \quad (\text{A4})$$

with φ_i and ε_i denoting the Kohn-Sham orbitals and energies, respectively, one can see that the self-energy term takes the place of the exchange-correlation potential v_{xc} .

As a starting point, the Kohn-Sham energies and wave function were determined self-consistently within the LDA. Then, the quasiparticle effects enter the calculations as energy corrections, obtained using first-order perturbation theory to evaluate the operator $(\Sigma - v_{xc})$ at the Kohn-Sham energies and for the Kohn-Sham wave functions.

All defect-energy level calculations in this paper are carried out with the ABINIT (Refs. 47–50) software package. The density functional theory simulations are performed for the crystal at zero temperature. We use Vanderbilt ultrasoft pseudopotentials,⁵¹ as, according to our calculations, the band gap energy differs only by 0.1 eV from the value obtained with norm-conserving pseudopotentials. For the generation of the pseudopotentials, the following reference configurations were used: For oxygen, we include all six electrons in the $n = 2$ shell ($2s^2 2p^4$). For zirconium, all electrons in the $n = 4$ shell plus the $5s$ electrons ($4s^2 4p^6 4d^2 5s^2 = 12$ electrons) were treated as valence electrons. Exchange and correlation are described using the Perdew-Zunger-Ceperley-Alder potential.^{52,53} Quasiparticle corrections for the highest occupied valence-band state and the lowest-lying CB state are calculated using the GW approximation. We apply the one-shot G_0W_0 approximation using the standard plasmon-pole model of Godby and Needs⁵⁴ at two frequencies: the static limit (0 eV) and another frequency, imaginary, on the order of the plasmon frequency (the peak in the electron energy-loss spectrum). We use the volume plasmon-pole energy of 13.8 eV given in Ref. 55.

First, we determine the energy gap of $t\text{-ZrO}_2$ using the same $2 \times 2 \times 2$ supercell consisting of 96 atoms that is used for the defect calculations. Note that the cell (as well as all defect supercells used in the calculations below) was relaxed

using a different ultrasoft pseudopotential (the volume per unit formula differs by less than $\sim 1\%$). The relative error caused by this is assumed to cancel in the final results as we are only interested in the positions of the defect states within the gap. The valence pseudowave functions are expanded in a projector-augmented-wave⁵⁶ basis set up to a kinetic energy of 15 hartree. In the screening calculation and in the calculation of the self-energy matrix elements, the summation is performed over 730 and 700 electronic bands, respectively. That is, in order to obtain converged GW results, about 350 unoccupied buffer bands were included in the summation. The calculation is carried out only at the Γ point. All parameters are converged within 0.1 eV. As a result, we obtain a LDA energy gap of 3.52 eV and a GW gap of 5.52 eV, which are used as a reference.

2. kMC

kMC provides a rigorous stochastic framework to simulate transport at the level of single-charge carriers. Full real-time dynamics of the charge carriers is taken into account. It offers the unique ability to model the statistical interplay between different intertwined microscopic processes, in our case, the different transport mechanisms relevant for electron conduction in high- κ thin-film capacitors.

In order to accurately describe the dynamics of a system, in this case, the TZAZT capacitor, the system is regarded as an entity, which, for every instant of time, can be characterized by its macroscopic state, here defined by the distribution of electrons within the dielectric. Within the electrodes, a continuous Fermi-Dirac distribution of the charge carriers is assumed.²⁸ Different system states are connected with each other via state-to-state transitions. In our case, the movement of a single electron is to be understood as such a transition. All types of transitions taken into account in the present kMC simulations are listed in Sec. III and are sketched in Fig. 4. A transition rate R is associated with every transition, whereas R is proportional to the probability of the transition. Usually, it is assumed that the rate R_{ij} for a transition from state i to state j does not depend on the system's prehistory. This means that the system has no memory on how it reached state i . The time evolution of such a system is governed by the master equation,

$$\frac{dP_i(t)}{dt} = - \sum_{j \neq i} R_{ij} P_i(t) + \sum_{j \neq i} R_{ji} P_j(t), \quad (\text{A5})$$

whereas $P_i(t)$ is the probability to find the system at time t in state i . Essentially, kMC models the time evolution by solving

the system's master equation in a stochastic framework. This often is favorable, since the number of possible states can be huge, and their interrelation complex, and an analytical solution of Eq. (A5) is not feasible. kMC offers a rigorous procedure to correctly propagate the system from state to state or, in this case, to compute a single-electron trajectory, describing the passage of an electron through the dielectric film.

Let us briefly describe the design of a kMC algorithm. Every simulation starts by defining the initial macroscopic state, i.e., the electron distribution. In the next step, a list of all possible transitions from this state to other system states is compiled, and the corresponding transition rates are calculated according to the supplied models (taken from Ref. 13). The kMC algorithm, as implemented, provides procedures to, in a statistical sense, correctly choose the next transition and to compute the time Δt , after which the transition should be carried out. According to Refs. 57 and 58, Δt and the next system state μ , to which the system is propagated, can be determined from

$$\Delta t = -\ln(r_1)/R_{\text{tot}}, \quad (\text{A6})$$

and

$$\sum_{\mu'=1}^{\mu-1} R_{\mu'}/R < r_2 \leq \sum_{\mu'=1}^{\mu} R_{\mu'}/R, \quad (\text{A7})$$

whereas $R_{\text{tot}} = \sum_{i=1}^N R_i$ is the cumulative transition rate of the N possible transitions. Thus, the essential kMC step is cut down to the generation of two random numbers r_1 and r_2 from the uniform distribution in the unit interval. After this is performed, the system is propagated to state μ , and the simulation time is incremented by Δt . The next kMC iteration is started by recompiling the list of possible transitions. This list may have changed due to the last transition since the system is now in another state. From this point, one proceeds as described above until the user-specified abortion conditions are fulfilled and the kMC simulation is terminated.

If a large number of single-electron trajectories is computed, the macroscopic transport properties evolve automatically. Mathematically, the average over many of such trajectories constitutes a numerical solution of the master equation that governs the system dynamics.⁵⁹ By simulating the transport of many electrons at the same time, charge-carrier interaction is included naturally in the simulation. More details for the kMC procedure can be found in Ref. 28.

*guntherjegert@mytum.de

[†]Previous address: Walter Schottky Institute, TU Munich, D-85748 Garching, Germany.

¹E. G. Seebauer and M. C. Kratzer, *Mater. Sci. Eng. R* **55**, 57 (2006).

²M. Levinson, M. Stavola, J. L. Benton, and L. C. Kimerling, *Phys. Rev. B* **28**, 5848 (1983).

³P. E. Blöchl, *Phys. Rev. B* **62**, 6158 (2000).

⁴P. Broqvist and A. Pasquarello, *Appl. Phys. Lett.* **89**, 262904 (2006).

⁵J. Kavalieros, B. Doyle, S. Datta, G. Dewey, M. Doczy, B. Jin, D. Lionberger, M. Metz, W. Rachmady, M. Radosavljevic, U. Shah, N. Zelik, and R. Chau, *2006 Symposium on VLSI Technology*, 2006. *Digest of Technical Papers* (IEEE, Piscataway, NJ, 2006), p. 50.

- ⁶A. Javey, H. Kim, M. Brink, Q. Wang, A. Ural, J. Guo, P. McIntyre, P. McEuen, M. Lundstrom, and H. Dai, *Nature Mater.* **1**, 241 (2002).
- ⁷S. Monaghan, K. Cherkaoui, É. O'Connor, V. Djara, P. K. Hurley, L. Oberbeck, E. Tois, L. Wilde, and S. Teichert, *IEEE Electron. Device Lett.* **30**, 219 (2009).
- ⁸J. Robertson, *Eur. Phys. J. Appl. Phys.* **28**, 265 (2004).
- ⁹K. Xiong, J. Robertson, M. C. Gibson, and S. J. Clark, *Appl. Phys. Lett.* **87**, 183505 (2005).
- ¹⁰J. Robertson, K. Xiong, and B. Falabretti, *IEEE Trans. Device Mater. Reliab.* **5**, 84 (2005).
- ¹¹D. Ricci, G. Bano, G. Pacchioni, and F. Illas, *Phys. Rev. B* **68**, 224105 (2003).
- ¹²T. S. Bjorheim, S. Stolen, and T. Norby, *Phys. Chem. Chem. Phys.* **2**, 6817 (2010).
- ¹³G. Jegert, A. Kersch, W. Weinreich, U. Schröder, and P. Lugli, *Appl. Phys. Lett.* **96**, 062113 (2010).
- ¹⁴Y. Seo, S. Lee, I. An, C. Song, and H. Jeong, *Semicond. Sci. Technol.* **24**, 115016 (2009).
- ¹⁵S. Ramanathan, C.-M. Park, and P. McIntyre, *J. Appl. Phys.* **91**, 4521 (2002).
- ¹⁶R. Chau, B. Doyle, S. Datta, J. Kavalieros, and K. Zhang, *Nature Mater.* **6**, 810 (2007).
- ¹⁷[www.itrs.net/links/2010itrs/home2010.htm].
- ¹⁸S. Schmelzer, D. Brauhaus, S. Hoffmann-Eifert, P. Meuffels, U. Böttger, L. Oberbeck, P. Reinig, U. Schröder, and R. Waser, *Appl. Phys. Lett.* **97**, 132907 (2010).
- ¹⁹K. M. Rabe, *Nat. Nanotechnol.* **1**, 171 (2006).
- ²⁰C. J. Först, C. R. Ashman, K. Schwarz, and P. E. Blöchl, *Nature (London)* **427**, 53 (2004).
- ²¹S. K. Kim, G.-J. Choi, S. Y. Lee, M. Seo, S. W. Lee, J. H. Han, H.-S. Ahn, S. Han, and C. S. Hwang, *Adv. Mater.* **20**, 1429 (2008).
- ²²H. J. Cho, Y. D. Kim, D. S. Park, E. Lee, C. H. Park, J. S. Jang, K. B. Lee, H. W. Kim, Y. J. Ki, I. K. Han, and Y. W. Song, *Solid-State Electron.* **51**, 1529 (2007).
- ²³Y.-H. Wu, C.-K. Kao, B.-Y. Chen, Y.-S. Lin, M.-Y. Li, and H.-C. Wu, *Appl. Phys. Lett.* **93**, 033511 (2008).
- ²⁴D. Zhou, U. Schröder, J. Xu, J. Heitmann, G. Jegert, W. Weinreich, M. Kerber, S. Knebel, E. Erben, and T. Mikolajick, *J. Appl. Phys.* **108**, 124104 (2010).
- ²⁵D.-S. Kil, H.-S. Song, K.-J. Lee, K. Hong, J.-H. Kim, K.-S. Park, S.-J. Yeom, J.-S. Roh, N.-J. Kwak, H.-C. Sohn, J.-W. Kim, and S.-W. Park, *2006 Symposium on VLSI Technology. Digest of Technical Papers 2006* (IEEE, Piscataway, NJ, 2006).
- ²⁶G. Jegert, A. Kersch, W. Weinreich, and P. Lugli, *J. Appl. Phys.* **109**, 014504 (2011).
- ²⁷K. Xiong, Y. Du, K. Tse, and J. Robertson, *J. Appl. Phys.* **101**, 024101 (2007).
- ²⁸G. Jegert, A. Kersch, W. Weinreich, and P. Lugli, *IEEE Trans. Electron Devices* **58**, 327 (2011).
- ²⁹L. Hedin and S. Lundqvist, *Solid State Phys.* **23**, 1 (1970).
- ³⁰L. Jönsson, W. G. Aulbur, and J. W. Wilkins, *Solid State Phys.* **54**, 1 (1999).
- ³¹M. Shishkin and G. Kresse, *Phys. Rev. B* **75**, 235102 (2007).
- ³²J. Thorp, A. Aypar, and J. S. Ross, *J. Mater. Sci.* **7**, 729 (1972).
- ³³C.-G. Zhan, J. A. Nichols, and D. A. Dixon, *J. Phys. Chem. A* **107**, 4184 (2003).
- ³⁴P. Rinke, A. Janotti, M. Scheffler, and C. G. Van de Walle, *Phys. Rev. Lett.* **102**, 026402 (2009).
- ³⁵D. Muñoz Ramo, P. V. Sushko, J. L. Gavartin, and A. L. Shluger, *Phys. Rev. B* **78**, 235432 (2008).
- ³⁶A. S. Foster, V. B. Sulimov, F. Lopez Gejo, A. L. Shluger, and R. M. Nieminen, *Phys. Rev. B* **64**, 224108 (2001).
- ³⁷B. Kralik, E. K. Chang, and S. G. Louie, *Phys. Rev. B* **57**, 7027 (1998).
- ³⁸X. Urli, C. L. Dias, L. J. Lewis, and S. Roorda, *Phys. Rev. B* **77**, 155204 (2008).
- ³⁹G.-M. Rignanese, F. Detraux, X. Gonze, and A. Pasquarello, *Phys. Rev. B* **64**, 134301 (2001).
- ⁴⁰W. Weinreich, R. Reiche, M. Lemberger, G. Jegert, J. Müller, L. Wilde, S. Teichert, J. Heitmann, E. Erben, L. Oberbeck, U. Schröder, A. J. Bauer, and H. Ryssel, *Microelectron. Eng.* **86**, 1826 (2009).
- ⁴¹J. Robertson, *Phys. Status Solidi A* **207**, 261 (2010).
- ⁴²J. Robertson, *J. Vac. Sci. Technol. B* **18**, 1785 (2000).
- ⁴³D. Liu and J. Robertson, *Appl. Phys. Lett.* **94**, 042904 (2009).
- ⁴⁴G. Lucovsky, D. M. Fleetwood, S. Lee, H. Seo, R. D. Schrimpf, J. A. Felix, J. Lüning, L. B. Fleming, M. Ulrich, and D. E. Aspnes, *IEEE Trans. Nucl. Sci.* **53**, 3644 (2006).
- ⁴⁵D. Martin, M. Grube, W. M. Weber, J. Rüstig, O. Bierwagen, L. Geelhaar, and H. Riechert, *Appl. Phys. Lett.* **95**, 142906 (2009).
- ⁴⁶G. Lucovsky, C. C. Fulton, Y. Zhang, Y. Zou, J. Luning, L. F. Edge, J. L. Whitten, R. J. Nemanich, H. Ade, D. G. Schlom, V. V. Afanasev, A. Stesmans, S. Zollner, D. Triyoso, and B. R. Rogers, *IEEE Trans. Device Mater. Reliab.* **5**, 65 (2005).
- ⁴⁷M. Torrent, F. Jollet, F. Bottin, G. Zérah, and X. Gonze, *Comput. Mater. Sci.* **42**, 337 (2008).
- ⁴⁸X. Gonze, G.-M. Rignanese, M. Verstraete, and J. M. Beuken, *Z. Kristallogr.* **220**, 458 (2005).
- ⁴⁹X. Gonze *et al.*, *Comput. Phys. Commun.* **180**, 2582 (2009).
- ⁵⁰X. Gonze, J.-M. Beuken, R. Caracas, F. Detraux, M. Fuchs, G.-M. Rignanese, L. M. Sindic, M. J. Verstraete, G. Zerah, F. Jollet, M. Torrent, A. Roy, M. Mikami, P. Ghosez, J.-Y. Raty, and D. C. Allan, *Comput. Mater. Sci.* **25**, 478 (2002).
- ⁵¹D. Vanderbilt, *Phys. Rev. B* **41**, 7892 (1990).
- ⁵²J. P. Perdew and A. Zunger, *Phys. Rev. B* **23**, 5048 (1981).
- ⁵³D. M. Ceperley and B. J. Alder, *Phys. Rev. Lett.* **45**, 566 (1980).
- ⁵⁴R. W. Godby and R. J. Needs, *Phys. Rev. Lett.* **62**, 1169 (1989), and references therein.
- ⁵⁵K.-O. Axelsson, K.-E. Keck, and B. Kasemo, *Surf. Sci.* **164**, 109 (1985).
- ⁵⁶P. E. Blöchl, *Phys. Rev. B* **50**, 17953 (1994).
- ⁵⁷K. A. Fichthorn and W. H. Weinberg, *J. Chem. Phys.* **95**, 1090 (1991).
- ⁵⁸D. T. Gillespie, *J. Comput. Phys.* **22**, 403 (1976).
- ⁵⁹K. Reuter, *Modeling Heterogeneous Catalytic Reactions: From the Molecular Process to the Technical System*, edited by O. Deutschmann (Wiley-VCH, Weinberg, 2009).